Temporal Variability of Diapycnal Mixing in Shag Rocks Passage

GILLIAN M. DAMERELL AND KAREN J. HEYWOOD

School of Environmental Sciences, University of East Anglia, Norwich, United Kingdom

DAVID P. STEVENS

School of Mathematics, University of East Anglia, Norwich, United Kingdom

ALBERTO C. NAVEIRA GARABATO

School of Ocean and Earth Science, National Oceanography Centre, Southampton, United Kingdom

(Manuscript received 8 September 2010, in final form 13 September 2011)

ABSTRACT

Diapycnal mixing rates in the oceans have been shown to have a great deal of spatial variability, but the temporal variability has been little studied. Here results are presented from a method developed to calculate diapycnal diffusivity from moored acoustic Doppler current profiler (ADCP) velocity shear profiles. An 18-month time series of diffusivity is presented from data taken by a LongRanger ADCP moored at 2400-m depth, 600 m above the seafloor, in Shag Rocks Passage, a deep passage in the North Scotia Ridge (Southern Ocean). The Polar Front is constrained to pass through this passage, and the strong currents and complex topography are expected to result in enhanced mixing. The spatial distribution of diffusivity in Shag Rocks Passage deduced from lowered ADCP shear is consistent with published values for similar regions, with diffusivity possibly as large as 90×10^{-4} m^2 s^{-1} near the seafloor, decreasing to the expected background level of $\sim 0.1 \times 10^{-4}$ m^2 s^{-1} in areas away from topography. The moored ADCP profiles spanned a depth range of 2400–1800 m; thus, the moored time series was obtained from a region of moderately enhanced diffusivity.

The diffusivity time series has a median of 3.3×10^{-4} m^2 s^{-1} and a range from 0.5×10^{-4} to 57×10^{-4} m^2 s^{-1}. There is no significant signal at annual or semiannual periods, but there is evidence of signals at periods of approximately 14 days (likely due to the spring–neap tidal cycle) and at periods of 3.8 and 2.6 days most likely due to topographically trapped waves propagating around the local seamount. Using the observed stratification and an axisymmetric seamount, of similar dimensions to the one west of the mooring, in a model of baroclinic topographically trapped waves, produces periods of 3.8 and 2.6 days, in agreement with the signals observed. The diffusivity is anticorrelated with the rotary coefficient (indicating that stronger mixing occurs during times of upward energy propagation), which suggests that mixing occurs due to the breaking of internal waves generated at topography.

1. Introduction

Diapycnal mixing is considered to be an important component of the three-dimensional ocean circulation (Wunsch and Ferrari 2004). A global average diapycnal diffusivity κ_z of approximately 10^{-4} m^2 s^{-1} is required to maintain the abyssal stratification (Munk and Wunsch 1998). Measurements in the ocean interior, away from boundaries and complex topography, have typically found κ_z $O(0.1 \times 10^{-4}\,\text{m}^2\,\text{s}^{-1})$ (Toole et al. 1994; Ledwell et al. 1998; Kunze et al. 2006), whereas in areas with strong currents and complex topography diffusivities can be several orders of magnitude larger (Polzin et al. 1997; Mauritzen et al. 2002; Naveira Garabato et al. 2004; Sloyan 2005). However, most existing measurements or estimates of diffusivity are either snapshots at a single time or a single integrated value over months or years. The few time series available, such as those discussed by Inall et al. (2000), Rippeth et al. (2002), Palmer et al. (2008), Moum and Nash (2009), and Shroyer et al. (2010), are from shallow shelf seas or tidal channels and cover

Corresponding author address: Gillian Damerell, School of Environmental Sciences, University of East Anglia, Norwich NR4 7TJ, United Kingdom.
E-mail: g.damerell@uea.ac.uk

DOI: 10.1175/2011JPO4573.1

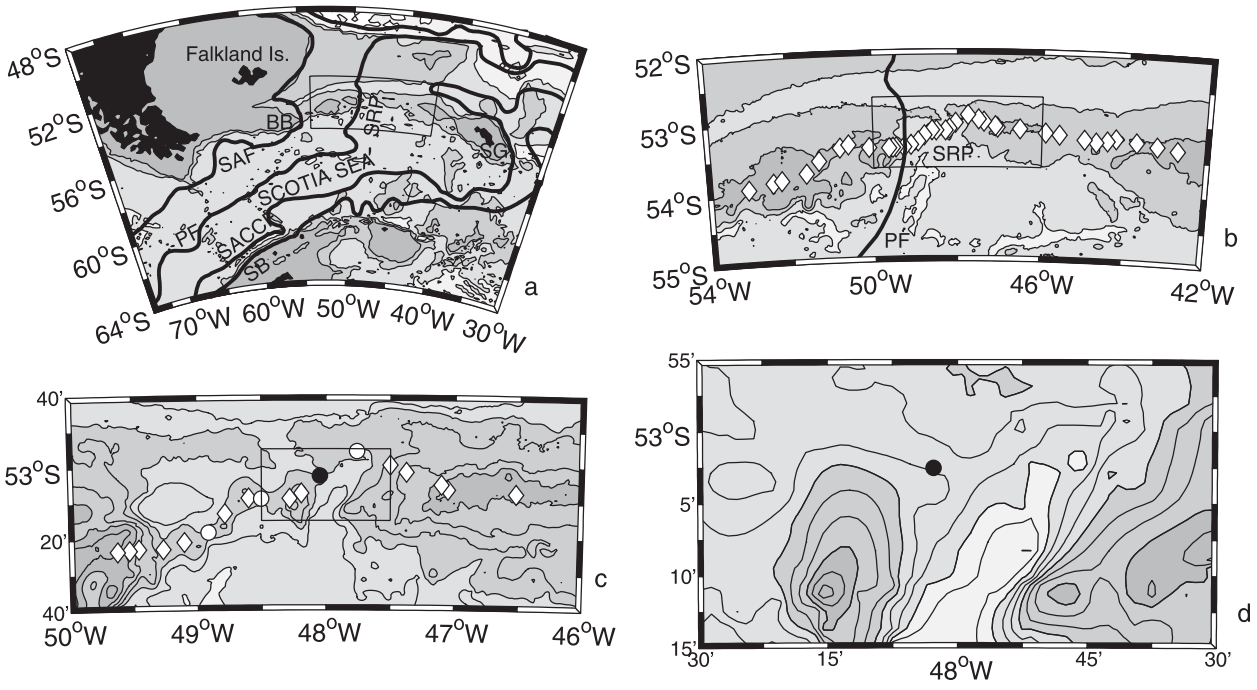

FIG. 1. Regional map, with bathymetry from Smith and Sandwell (1997), and climatological trajectories of the ACC fronts from Orsi et al. (1995): [Subantarctic Front (SAF), Polar Front (PF), Southern ACC Front (SACCF), Southern boundary of the ACC (SB)]. The following topographic features are indicated by their initials: Burdwood Bank (BB), South Georgia (SG), Shag Rocks Passage (SRP). (a) Overview of the Scotia Sea and (b) North Scotia Ridge with deployment cruise station locations indicated by diamonds. Contour intervals are every 1500 m in (a),(b). (c) Overview of Shag Rocks Passage. Contour intervals are now every 500 m with shading every 1500 m. The circles are the mooring locations at which CTDs were deployed during both the deployment and recovery cruises; other deployment cruise station locations are indicated by diamonds. From west to east, the moorings are Shag1a, Shag1b, Shag2 (a and b) and Shag3 (a and b). This study is concerned primarily with mooring Shag2b, which is the black circle. (d) Shag Rocks Passage: contour intervals are now every 200 m with shading every 600 m. The black circle is mooring Shag2b. Note the seamount of height ~1600 m southeast of the mooring location. In (a),(b) and (c), the thin black rectangle indicates the area shown in the next panel.

only a few days or weeks, with the longest (Moum and Nash 2009) spanning a period of 4 months.

Here we present a method that could, if applied widely, begin to address the question of whether single estimates in the deep ocean can be considered representative of long-term values. We derive an 18-month time series of the rate of dissipation of turbulent kinetic energy ϵ and κ_z and discuss some possible mechanisms for the temporal variability seen in these series.

The Scotia Sea, an area of complex topography on the eastern side of Drake Passage (Fig. 1a), has been the focus of a number of studies considering mixing rates (Heywood et al. 2002; Naveira Garabato et al. 2003, 2004). Here, the Subantarctic Front (SAF) and Polar Front (PF) veer northward over the ~2000-km-long North Scotia Ridge, where the shallow (200–2000 m) topography presents an obstacle to the circumpolar flow of deep waters. The Polar Front is constrained to cross the ridge through Shag Rocks Passage (SRP), a 180-km-wide, 3200-m-deep fracture zone between 49.6° and 47.1°W (Moore et al. 1997; Arhan et al. 2002).

As part of the North Scotia Ridge Overflow Project (Smith et al. 2010), conductivity–temperature–depth (CTD) and lowered acoustic Doppler current profiler (LADCP) profiles were collected between 23 April and 5 May 2003 along the length of the North Scotia Ridge (Fig. 1). Six moorings were placed in Shag Rocks Passage between April 2003 and November 2004 (Walkden et al. 2008), one of which (mooring Shag 2b, water depth 3000 m) included an upward-looking LongRanger ADCP 600 m above bottom (mab) (Table 1 and Fig. 1). The ADCP recorded velocity in 40 bins with a thickness of 16 m, thus observing a total depth of 640 m.

We calculate an 18-month κ_z time series using the method previously used in the Scotia Sea by Naveira Garabato et al. (2004), originally developed by Gregg and Kunze (1991), with further modifications following Polzin et al. (2002) and Gregg et al. (2003), wherein κ_z can be estimated from profiles of temperature, salinity, and current velocity. This relies on the premise that the nonlinear interactions of internal waves initiate an energy cascade to smaller scales, resulting in turbulent

TABLE 1. Instruments moored in Shag Rocks Passage from 6 May 2003 to 27 Nov 2004: mab indicates meters above bottom.

Mooring	Lat	Lon	Depth (m)	Instrument	mab	Sampling interval
Shag 1a	53°18.251′S	48°54.828′W	2960	Aanderaa RCM8	30	hourly
Shag 1b	53°09.018′S	48°29.948′W	2766	Aanderaa RCM8	400	hourly
				RDI 300-kHz Workhorse ADCP	600	20 min
				Pressure/temperature logger XR420 TD	600	3 min
Shag 2a	53°02.510′S	48°02.313′W	2996	Aanderaa RCM8	30	hourly
				Aanderaa RCM8	100	hourly
Shag 2b	53°02.510′S	48°02.770′W	2999	Aanderaa RCM8	400	hourly
				RDI 75 kHz LongRanger ADCP	600	2-hourly
				Pressure/temperature logger SBE-39	600	10 min
Shag 3a	52°55.653′S	47°45.992′W	2928	Aanderaa RCM8	30	hourly
				Aanderaa RCM8	100	hourly
Shag 3b	52°55.670′S	47°45.550′W	2945	Aanderaa RCM8	400	hourly
				RDI 300-kHz Workhorse ADCP	600	20 min

dissipation (McComas and Muller 1981; Henyey et al. 1986) from which κ_z can be inferred (Osborn 1980). This method can therefore only assess mixing due to internal wave breaking (and not that due to other noninternal wave processes). This is a valid assumption for this region since the instruments are not in a region where waters are cascading over a sill, are 600 m off the seafloor, so should be away from bottom boundary layers that might be dominated by bottom friction, and are observing water deep enough (>1800 m) that direct wind-driven mixing, such as occurs in the surface mixed layer, is unlikely to occur.

Possible mechanisms for internal wave generation include the following.

(i) Wind forcing can generate near-inertial motions, and, although the large inertial oscillations seen in near-surface waters decrease in amplitude rapidly with depth below the mixed layer (Pollard 1970; Pollard and Millard 1970), they do penetrate somewhat into the ocean interior as internal waves (D'Asaro 1984; Alford 2001, 2003a,b). These could then interact further with the local topography, much of which is only a few hundred meters deep along the North Scotia Ridge.

(ii) In stratified waters, the interaction of barotropic tidal currents with variable bottom topography can result in the generation of internal tides (Heywood et al. 2007). As discussed by Garrett and St. Laurent (2002), St. Laurent and Garrett (2002), and Garrett and Kunze (2007), most of the energy flux is associated with low modes that propagate away from the generation region, but intense beams of internal tidal energy are generated by certain ''critical'' slopes and lead to local mixing.

(iii) In principle, any movement of water over rough topography may generate internal waves (Bell 1975; Baines 1982), which can then initiate an energy cascade to smaller scales and cause turbulent dissipation (McComas and Muller 1981; Henyey et al. 1986). As well as internal tides, this can be through the generation of lee waves by geostrophic flows (Nikurashin and Ferrari 2010a,b), particularly in the Southern Ocean where bottom geostrophic flows are much more intense than in most other ocean basins. The complex topography in Shag Rocks Passage (Fig. 1d) includes many features at which lee waves could be generated.

(iv) The mean flow can also interact with the internal wave field. For example, Kunze and Sanford (1984) and Kunze (1985) observed intense, focused beams of downward propagating near-inertial waves at the base of regions of upper-ocean negative vorticity. They determined that a wave-mean flow interaction model, which predicts trapping and amplification of near-inertial waves in regions of negative vorticity, best explained their observations.

The generation from, and interaction with, geostrophic flows may also lead to another indirect link between internal waves and wind forcing, as increased wind speeds can lead to intensified currents or result in increased eddy activity that transmits momentum downward through the water column (Bryden 1979; Olbers 1998).

The organization of this paper is as follows: Section 2 begins with a description of the method and uses this to

produce a section of κ_z along the North Scotia Ridge, thus setting the spatial context for the moored time series. Section 3 discusses the modifications to the method for use with mooring data and the time series thus obtained. In section 4, spectral analysis is used to identify significant periodicities, and potential sources of temporal variability in κ_z are identified. Section 5 presents the conclusions.

2. Spatial variability of diffusivity in Shag Rocks Passage

First, we recap the methodology used by several authors (e.g., Polzin et al. 1995, 2002; Naveira Garabato et al. 2004; Kunze et al. 2006) to estimate ϵ and κ_z from LADCP data. Estimates of κ_z are inferred from velocity shear estimates using a model that assumes a statistical balance between turbulent production, buoyancy flux, and dissipation (Osborn 1980). In common with previous LADCP analyses, we assume that subinertial shear is small compared with that in the internal wave field. The dissipation rate and diapycnal diffusivity are related by $\kappa_z = \Gamma\epsilon/N^2$, where Γ is the mixing efficiency (generally assumed to be 0.2) and N is the buoyancy frequency. The turbulent dissipation rate can be found from

$$\epsilon = \epsilon_0 \times \frac{f}{f_0}\frac{N^2}{N_0^2}\frac{\cosh^{-1}(N/f)}{\cosh^{-1}(N_0/f_0)}\frac{\langle V_z^2\rangle^2}{\langle V_{z-\mathrm{GM}}^2\rangle^2}h_1(R_\omega) \quad (1)$$

(Gregg and Kunze 1991; Polzin et al. 1995, 2002; Gregg et al. 2003). Here $\epsilon_0 = 7.8 \times 10^{-10}$ W kg^{-1} is the turbulent dissipation rate of the background internal wave field in stratification defined by a buoyancy frequency $N_0 = 5.24 \times 10^{-3}$ rad s^{-1} at a latitude of 30°, as predicted for the Garrett and Munk (GM) model (Garrett and Munk 1975); f and f_0 are the inertial frequencies at the latitude of observation and at 30°, respectively ($f_0 = 7.3 \times 10^{-5}$ s^{-1} and $f = 1.2 \times 10^{-4}$ s^{-1}). The latitudinal dependence of the energy cascade to smaller scales is discussed by Gregg et al. (2003). In (1) $\langle V_z^2\rangle$ is the variance of the LADCP vertical shear, normalized by N, and $\langle V_{z-\mathrm{GM}}^2\rangle$ is the same variable, as predicted by the GM model; $h_1(R_\omega)$ is a function of the frequency content of the internal wave field (Polzin et al. 1995) estimated from the shear-to-strain ratio R_ω, discussed below.

To derive $\langle V_z^2\rangle$, each LADCP shear profile is divided into overlapping 320-m segments spaced at 100-m intervals and normalized by the average buoyancy frequency $\overline{N}$ for that segment. The normalized shear in each segment is Fourier transformed (64 points) to compute the vertical wavenumber power spectral density (PSD). This spectrum is corrected to account for the smoothing in the velocity profiles at high vertical wavenumbers caused by the spatial averaging inherent in LADCP measurement and data processing (Polzin et al. 2002). Specifically, the corrections described by Polzin et al. for the finite acoustic transmission and reception intervals, first differencing of the resulting single-ping velocity profiles, interpolation of the first-differenced profiles onto a regular depth grid, and instrument tilt are applied. $\langle V_z^2\rangle$ is calculated by integrating the corrected power spectral density between the maximum vertical wavelength of 300 m and a minimum vertical wavelength of 90 m, chosen to minimize the contamination by instrument noise that can occur at higher wavenumbers. This minimum vertical wavelength threshold is selected heuristically by examination of the shear spectra, and the resulting ϵ and κ_z are insensitive to the exact value. $\langle V_{z-\mathrm{GM}}^2\rangle$ is integrated over the same wavelength range as $\langle V_z^2\rangle$.

The shear/strain variance ratio R_ω is a measure of the internal wave field's frequency content (Kunze et al. 1990) and is used to parameterize the turbulent dissipation rate in Eq. (1). Here, R_ω is found from

$$R_\omega = \frac{\langle V_z^2\rangle}{\langle \xi_z^2\rangle} = 3 \times \frac{\langle V_z^2\rangle}{\langle V_{z-\mathrm{GM}}^2\rangle}\frac{\langle \xi_{z-\mathrm{GM}}^2\rangle}{\langle \xi_z^2\rangle} \quad (2)$$

in which $\langle \xi_z^2\rangle$ is the variance of strain, the vertical gradient of the vertical displacement of isopycnals induced by internal waves, and $\langle \xi_{z-\mathrm{GM}}^2\rangle$ is the same variable, as predicted by the GM model, and integrated over the same wavelength range as $\langle \xi_z^2\rangle$. The factor of 3 arises because $\langle V_{z-\mathrm{GM}}^2\rangle/\langle \xi_{z-\mathrm{GM}}^2\rangle = 3$. Strain is estimated from CTD density profiles using a scale separation assumption (Polzin et al. 1995), and $\langle \xi_z^2\rangle$ (and R_ω) are calculated in 320-m segments identical to the $\langle V_z^2\rangle$ bins. Then R_ω is averaged horizontally over all stations to give a profile that varies with depth but does not vary from station to station. For each depth segment $h_1(R_\omega)$ is calculated (Polzin et al. 1995) as

$$h_1 = \frac{3(R_\omega + 1)}{2\sqrt{2}R_\omega\sqrt{R_\omega - 1}}. \quad (3)$$

The average of R_ω throughout Shag Rocks Passage is 6.0, corresponding to $h_1(R_\omega) = 0.56$. At the depths observed by the mooring, the average R_ω is 7.6, giving $h_1(R_\omega) = 0.47$, and it is this value that is used to parameterize diffusivities calculated from the mooring data, as discussed below.

The κ_z section across Shag Rocks Passage produced from the CTD/LADCP profiles (Fig. 2) shows greatly enhanced κ_z at depth and over complex topography ($\sim 90 \times 10^{-4}$ m^2 s^{-1}), decreasing to a background level $< 0.1 \times 10^{-4}$ m^2 s^{-1} [consistent with the findings of

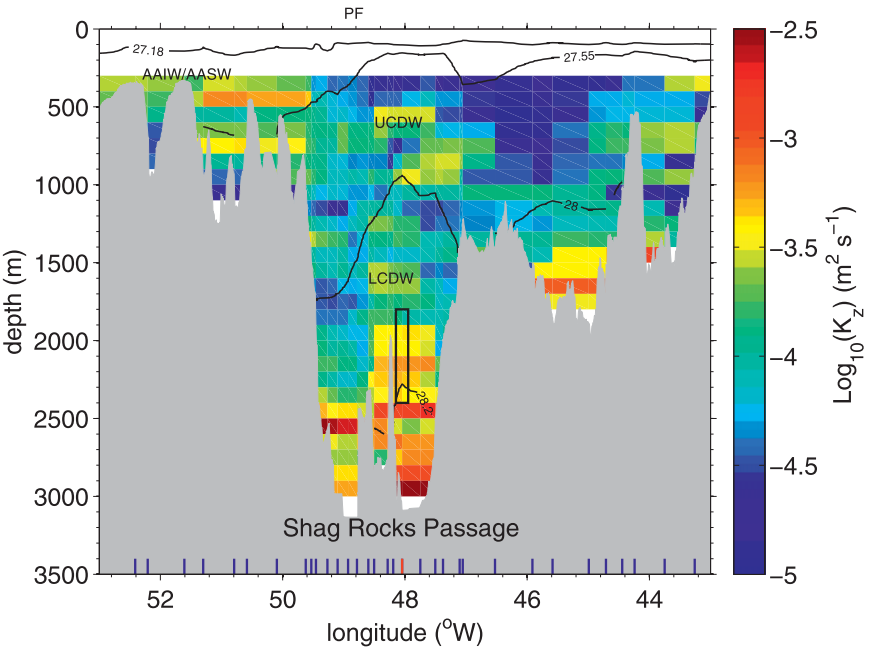

FIG. 2. Vertical diffusivity κ_z along the North Scotia Ridge. Density surfaces, shown as black lines, separate different water masses [Antarctic Intermediate Water/Antarctic Surface Water (AAIW/AASW), $27.18 < \gamma^n < 27.55$; Upper Circumpolar Deep Water (UCDW), $27.55 < \gamma^n < 28.00$; and Lower Circumpolar Deep Water (LCDW), $28.00 < \gamma^n < 28.20$: γ^n is the neutral density (kg m^{-3}) as defined by Jackett and McDougall (1997)]. Station positions are indicated by blue tick marks at the base of the topography, with the mooring position as a red tick mark. The approximate location of the PF is marked on the upper axis. The black rectangle in Shag Rocks Passage gives an approximate indication of the extent of the LongRanger ADCP at mooring Shag 2b; the horizontal extent of the rectangle is for illustrative purposes only.

Toole et al. (1994), Ledwell et al. (1998), and Kunze et al. (2006)] in areas well away from the seafloor and at depths of no more than 1000 m. Similarly ϵ varies between $\sim 0.02 \times 10^{-9}$ and 23×10^{-9} W kg^{-1} and has a comparable spatial pattern (not shown). Both κ_z and ϵ are smoothed horizontally using a five-station running mean. This section is comparable to published sections elsewhere, particularly those in and around the Scotia Sea (Naveira Garabato et al. 2004; Sloyan 2005). The Sloyan meridional section across the Scotia Sea (her Fig. 3a) is calculated using CTD strain variance techniques and shows $\kappa_z \sim 10 \times 10^{-4}$–$100 \times 10^{-4}$ m^2 s^{-1} near the seafloor, decreasing to $\sim 0.1 \times 10^{-4}$ m^2 s^{-1} or less away from rough topography, which is consistent with what is observed here.

The section of Naveira Garabato et al. (2004) shows $\kappa_z \sim 100 \times 10^{-4}$ m^2 s^{-1} near the seafloor, with a maximum of nearly 1000×10^{-4} m^2 s^{-1} at the seafloor of Drake Passage and in a deep gap (Orkney Passage) in the South Scotia Ridge (their Fig. 2). Fairly low values of $\sim 0.4 \times 10^{-4}$ to 4×10^{-4} m^2 s^{-1} were observed over the Falkland Plateau, geographically the closest region to the North Scotia Ridge. The much smoother topography of the Falkland Plateau compared with Shag Rocks Passage explains these lower values. The most similar region, in terms of roughness and depth of topography, is the South Scotia Ridge, which shows correspondingly similar results, including enhanced mixing over shallow (<1500-m depth) topography to the west of the South Orkney Islands, analogous to that seen in Fig. 2 to the west of Shag Rocks Passage. The considerably greater κ_z found by Naveira Garabato et al. in Orkney Passage (nearly 1000×10^{-4} m^2 s^{-1}) than seen anywhere in Shag Rocks Passage may be due to the stronger currents at the sea bed there [velocities approaching 50 cm s^{-1} (Naveira Garabato et al. 2002) as opposed to ~20 cm s^{-1} in Shag Rocks Passage]. Naveira Garabato et al. (2004) found a sharp reduction in κ_z to values only slightly above 0.1×10^{-4} m^2 s^{-1} in the uppermost 300–400 m of their section in Drake Passage, Orkney Passage, and the Scotia Sea. A similar pattern is seen in Fig. 2 between approximately 44° and 49°W. This region has comparable depths and roughness to the Drake Passage, Orkney Passage, and Scotia Sea sections of Naveira Garabato et al. (2004), which have comparable κ_z patterns.

Kunze et al. (2006) raised doubts about the applicability of the shear parameterization in very low abyssal

stratifications (their Fig. 3). They argue that noise in LADCP measurements prevents measurement of the shear in areas with $N < 4.5 \times 10^{-4}$ rad s^{-1}, casting doubt on the very high diffusivities at the seafloor of Naveira Garabato et al. (2004). Polzin and Lvov (2011) argue that what has previously been considered noise may in fact be a slow mode consisting of, at lowest order, the steady geostrophic balance. Higher order contributions are time dependence, nonlinearity, and the effects of a variable rate of planetary rotation (f). In the section presented here, $N > 4.5 \times 10^{-4}$ rad s^{-1}, except in a very small area below 2700 m east of the central seamount in Shag Rocks Passage. Moreover, we obtain similar values (not shown) from a strain-only calculation of κ_z independent of the LADCP shear, as used by Mauritzen et al. (2002) and Sloyan (2005). This strain-based calculation of κ_z gives a range from $\sim 0.05 \times 10^{-4}$ to 100×10^{-4} m^2 s^{-1} and a similar spatial pattern to κ_z calculated using LADCP shear. The shear parameterization should therefore be applicable to the moored ADCP time series.

The rotary coefficient (RC) of the vertical shear is the ratio of the clockwise and counterclockwise components of the shear variance and is a proxy for the ratio of upward to downward energy propagation. It is calculated following Gonella (1972) for the stations in Shag Rocks Passage deeper than 2000 m and lying to the east of the central seamount (Fig. 3). Above ~1500 m the propagation is mostly downward and most likely wind driven (Alford 2003a). Below ~1500 m the propagation is mostly upward, likely due to internal waves generated at the topography (Baines 1973, 1982; Thorpe 1992).

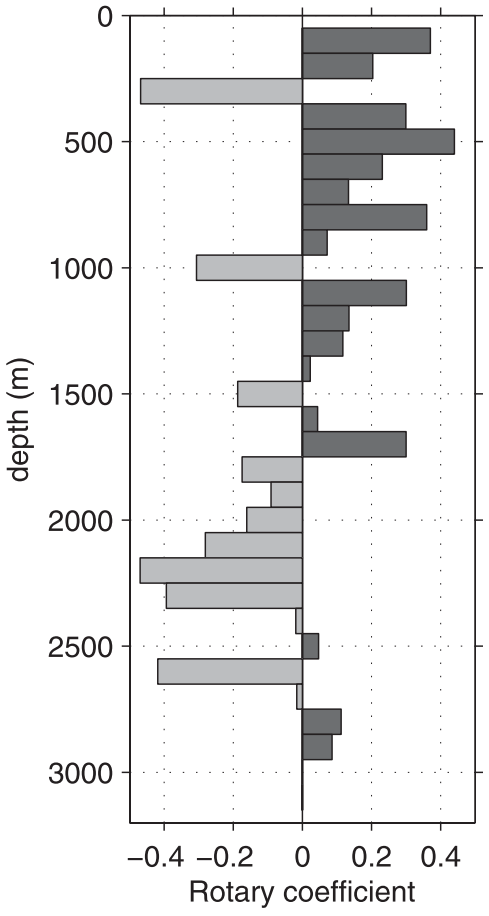

FIG. 3. Rotary coefficient (dimensionless) for the stations in Shag Rocks Passage deeper than 2000 m. Values less (greater) than zero indicate upward (downward) propagation of energy.

3. Temporal variability of diffusivity in Shag Rocks Passage

a. Methodology

The ADCP at mooring Shag2b produced time series of velocity profiles at 2-h intervals. The method adopted here to calculate κ_z for the time series is essentially the same as described in section 2 for the LADCP data, repeated for each time interval. There are some modifications to the calculations.

1) Depth segment and Fourier transform

The shears are treated as one 640-m segment centered at 2100-m depth. After quality control (which consisted of the rejection of points where less than 50% of the measurements had four-beam solutions), generally around 400–500 m remained for use in the Fourier transform and occasionally as little as 300 m. The quantity κ_z is insensitive to the chosen percentage for quality control; using either 25% or 75% as the rejection threshold makes a difference of around 4% to the calculated values, which is small compared with other uncertainties. Since the calculation requires depth bins of at least 320 m of good data, the data were not divided into depth segments in order to retain enough information to calculate the spectral densities. The ADCPs on moorings Shag1b and Shag3b (Table 1 and Fig. 1) recorded velocities in 23 bins of 8-m thickness. After quality control, insufficient depth range remained to resolve wavelengths of 90 m or more, so these could not be used to calculate κ_z.

Each velocity measurement of the ADCP on mooring Shag2b is based on 31 pings, corresponding to an accuracy of approximately 0.6 cm s^{-1}. The LADCP measurements are based on an average of ~120 pings, giving an accuracy of approximately 0.3 cm s^{-1}. In the stratification observed here (N typically $\sim 8 \times 10^{-4}$ to 9×10^{-4} s^{-1} in the CTD stations at the depths ensonified by the moored ADCP), typical internal wave speeds are ~1–5 cm s^{-1}

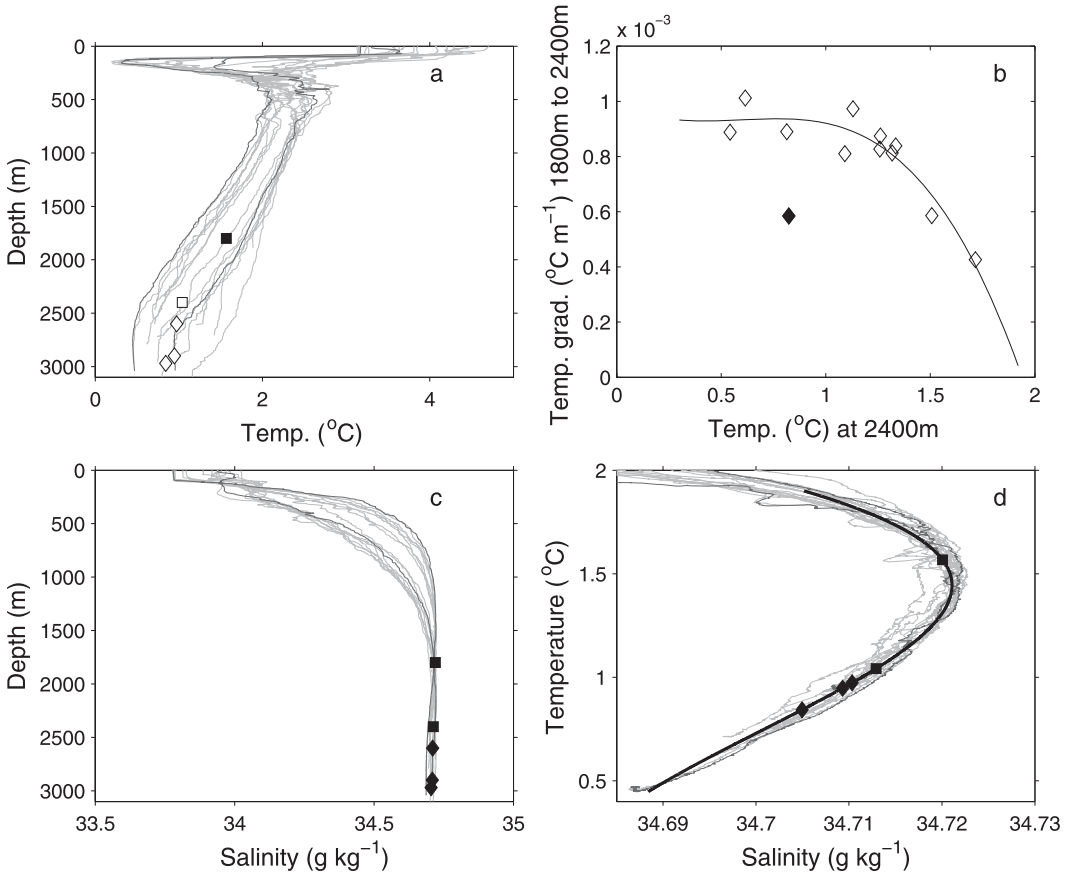

FIG. 4. Extrapolation of temperature and fitting for salinity used to derive the time series of buoyancy frequency: in (a),(c), and (d) the gray lines are profiles of the Shag Rocks Passage CTD stations, with the darker gray being the closest station of each cruise. (a) Temperature vs depth: the white diamonds are the mean temperatures recorded by the three RCMs at 30, 100, and 400 meters above bottom (mab); the white square is the mean temperature recorded by the sensor on the ADCP at 600 mab; and the black square is the mean extrapolated temperature at 1200 mab. (b) Relationship between the temperature at 2400 m and the temperature gradient between 1800 and 2400 m, the depth range observed by the moored ADCP: the black line is the cubic fit used to extrapolate temperatures above 2400 m during the mooring time series and the black diamond is station 58 of the deployment cruise, which was excluded as an outlier. (c) Salinity vs depth: the black diamonds and squares are the mean fitted salinities at 30, 100, 400, 600, and 1200 mab. (d) *T*–*S* relationship: the black line represents the cubic fit used to calculate salinity from temperature, and the black diamonds and squares represent the mean *T*–*S* values at 30, 100, 400, 600, and 1200 mab.

(Thorpe 2005), considerably greater than the accuracy of either instrument.

2) Buoyancy frequency

Time series of temperature and salinity were not measured in the volume of water above the mooring in which the currents are sampled by the ADCP. However, a SeaBird Electronics temperature sensor (SBE-39) was mounted on the ADCP, which has a comparable accuracy (±0.002°C) to the ship's CTD (SBE-3*plus*, accuracy ±0.001°C). Each rotary current meter (RCM; Table 1) recorded temperature with an accuracy of ±0.05°C. All moored temperature sensors agreed with CTD casts at the beginning and end of the mooring deployment. Here we discuss how best to use these time series to provide time series of temperature and salinity (and hence buoyancy frequency) appropriate to the water column monitored by the ADCP.

Thirteen full-depth CTD stations were occupied in Shag Rocks Passage during the deployment cruise, and four during the recovery cruise, that can be used to infer relationships between temperatures at different depths (Fig. 4). The four temperature time series from mooring Shag2 (a and b) are linearly related, as are the CTD temperatures at the same depths as the moored temperature sensors. Therefore, we fitted the CTD temperature gradient between 1800 and 2400 m (the depth range observed by the moored ADCP) to the temperature at 2400 m. Figure 4b illustrates the cubic fit that was found to best reproduce

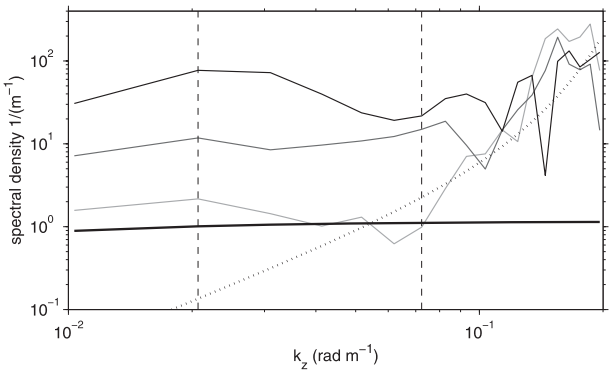

FIG. 5. Some example vertical wavenumber spectra. The thin solid lines are the spectra for the times when the calculated diffusivity was the minimum (pale gray), median (darker gray), and maximum (black) values of the time series. The thick solid black line is the GM model spectrum, and the dotted line is the spectrum for shear noise of velocity variance $(3.2\ \text{cm s}^{-1})^2$/nping, where nping is the number of pings used for each velocity measurement. The vertical dashed lines are the limits of integration, corresponding to wavelengths of 300 and 90 m.

the observed temperature profile. The CTD temperature profiles (Fig. 4a) fall into two groups: a warmer group and a colder group, which lie north and south of the Polar Front respectively. Stations with a higher temperature at 2400 m have a lower temperature gradient and vice versa (Fig. 4b). The spread in temperatures is thus less at 1800-m depth than at 2400 m. The cubic fit to the CTD stations was used, in conjunction with the temperature at 2400 m recorded by the ADCP, to generate temperature gradients and thus temperatures between 1800 and 2400 m for the entire time series.

Similarly, a cubic fit to the CTD in situ *T*–*S* relationship is used to infer salinities between 1800 and 2400 m (Fig. 4). From the temperatures and salinities a time series of buoyancy frequency is deduced. The parameter that has the greatest impact on the calculated κ_z is the temperature gradient, which varies by more than a factor of 10 during the time series. As is apparent in Fig. 4d, salinity varies by no more than 0.009 g kg^{-1} in the ADCP ensonified volume; the effect of salinity on the variability of κ_z is very small.

3) Spectral corrections

The corrections described by Polzin et al. (2002) for the finite acoustic transmission and reception intervals, as well as for first differencing of the resulting single-ping velocity profiles, are applied exactly as for the LADCP shear spectra. We do not need to apply the correction for interpolation of the first-differenced profiles onto a regular depth grid as no interpolation is performed for a moored instrument.

4) Smoothing

The finescale parameterization used here assumes a stationary internal wave field, and the stationarity assumption is more likely to hold over a time scale $> 1/f$ (15 h) than over 2 h. In a manner similar to the horizontal smoothing of κ_z and ϵ for the spatial section using a five-station running mean, here we calculate a running mean over 24 h for κ_z and ϵ. (The length of the running mean was chosen as a compromise between maintaining temporal resolution and the desire to justify the stationarity assumption.) All values quoted henceforth, or shown in figures or tables, will be those found after applying the running mean unless stated otherwise.

5) Shear-to-strain ratio parameterization

Since we do not have time series of temperature and salinity in the water mass ensonified by the ADCP, we cannot estimate $\langle \xi_z^2 \rangle$ as described in section 2 and thus cannot calculate a time series for R_ω. Instead, we use the average value of R_ω from the LADCP section over the ensonified depths, which gives $h_1(R_\omega) = 0.47$.

Some examples of the vertical wavenumber spectra of the shear are shown in Fig. 5 and are comparable to those in the literature (e.g., Fig. 2 of Kunze et al. 2006). Figure 5 also shows the vertical wavenumber spectrum for shear noise: rms noise levels are about (3.2 cm s^{-1})/nping$^{1/2}$ for a large number of scatterers (Polzin et al. 2002), where nping is the number of pings used for each velocity measurement. Over the interval of integration (90–300 m), the spectra are relatively flat and are clearly distinguishable from the noise spectrum. At higher wavenumbers (wavelengths $<$ 90 m), the spectra are dominated by noise, which illustrates the validity of the choice of 90 m as the minimum wavelength over which the spectra are integrated.

b. Resultant time series

Figure 6 shows the time series of ADCP velocity, integrated shear variance (ISV), temperatures, depth-average buoyancy frequency $\overline{N}$, rotary coefficient, and the derived κ_z. The integrated shear variance is $\langle V_z^2 \rangle$ without the normalization by $\overline{N}$, so as to show the shear and buoyancy frequency separately. Included for comparison is the 6-hourly wind speed from the European Centre for Medium-Range Weather Forecasts (ECMWF) Interim reanalysis dataset (ERA-Interim) (ECMWF 2009), at the nearest grid point (52.5°S, 48°W) to mooring Shag2b. All mooring time series show good agreement with the values obtained from the closest CTD/LADCP stations of the deployment and recovery cruises. The time series of ϵ is not shown,

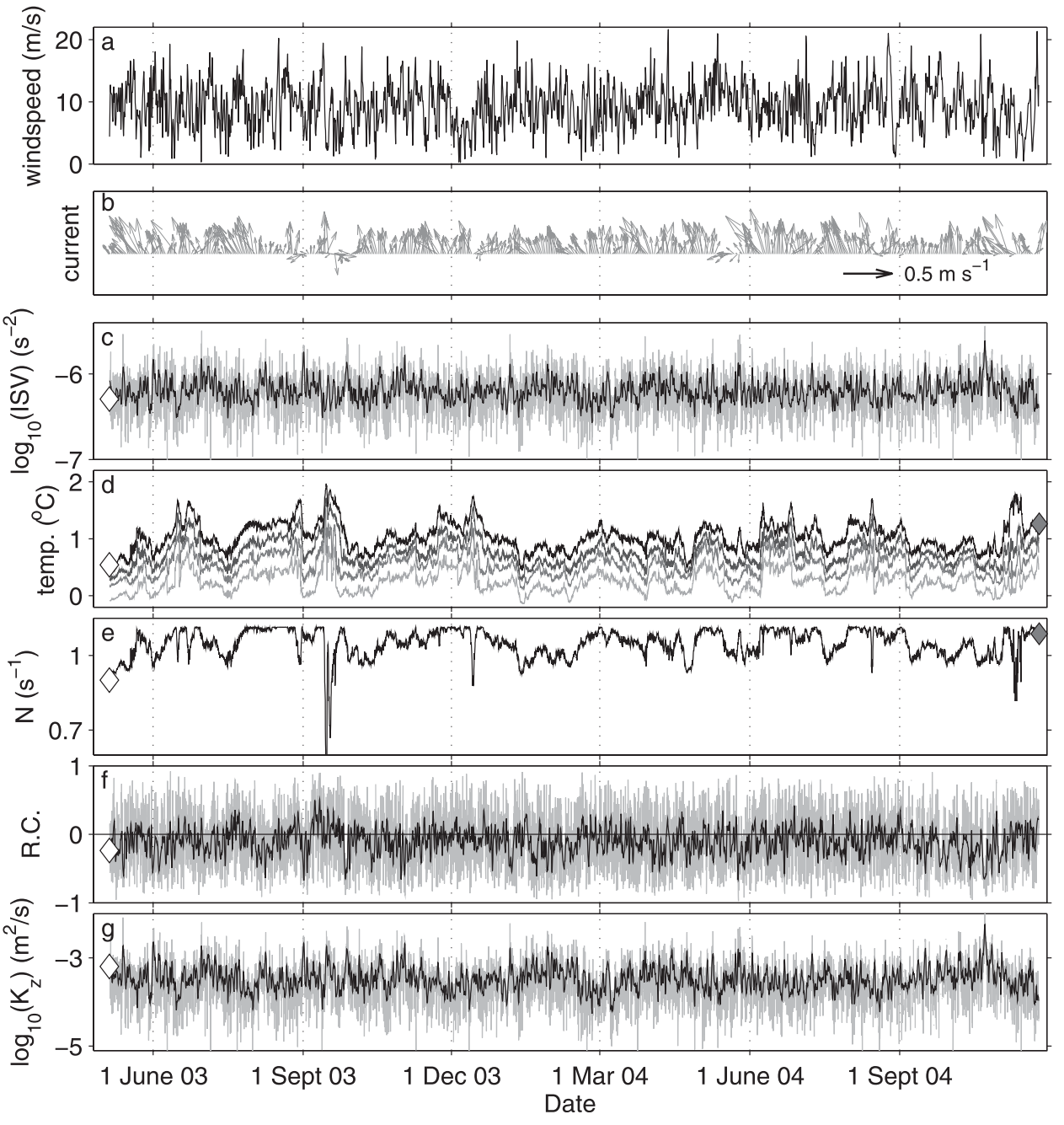

FIG. 6. Time series at the moored array in Shag Rocks Passage : (a) ECMWF reanalysis wind speed from the closest grid point; (b) depth-averaged daily currents recorded by the moored ADCP [the first arrow at the start of the time series is that recorded by the LADCP on the closest station of the deployment cruise (station 56)]; (c) $\log_{10}$ (ISV) (s^{-2}); and (d) temperature (°C) [the palest line is the temperature recorded 30 mab, offset by −0.6°C; the middle gray line is that recorded 100 mab, offset by −0.4°C; the darkest gray line is that recorded 400 mab, offset by −0.2°C; and the black line is that recorded 600 mab. The white diamond is that recorded by the CTD at station 56, and the gray diamond is that recorded by the CTD on the closest station of the recovery cruise (station 19), both at 2400 m]; (e) buoyancy frequency ($\times 10^{-3}$ s^{-1}) [the gray diamond (far right) is that recorded at station 19 of the recovery cruise, averaged over the depths observed by the moored ADCP]; (f) rotary coefficient (RC) (dimensionless); and (g) $\log_{10}(\kappa_z)$ (m^2 s^{-1}) (the horizontal line is the median value). For subplots (c) and (e)–(g), the gray line is the unsmoothed quantities; the black line is daily average values; and the white open diamond is that recorded at station 56 of the deployment cruise, averaged over the depths observed by the moored ADCP.

TABLE 2. Various statistics of the time series of integrated shear variance (ISV), buoyancy frequency $\overline{N}$, dissipation rate (ϵ), diffusivity (κ_z), and rotary coefficient (RC), with the equivalent values as found by the LADCP, taken from the nearest station of the deployment cruise and averaged over the same depths observed by the moored ADCP. All values are given to two significant figures, except for the buoyancy frequency, which is given to two decimal points in order to distinguish the median, 75th percentile, maximum, and mean. All time series values are after applying the running 24-h mean. The skewness and excess kurtosis are not scaled by the factors given in the column headings and are both dimensionless numbers.

	ISV ($\times 10^{-7}$ s^{-2})	$\overline{N}$ ($\times 10^{-3}$ s^{-1})	ϵ ($\times 10^{-9}$ W kg^{-1})	κ_z ($\times 10^{-4}$ m^2 s^{-1})	RC
Min	2.7	0.57	0.32	0.54	−0.68
25th percentile	5.3	1.01	1.3	2.2	−0.22
Median	6.2	1.05	1.8	3.3	−0.093
75th percentile	7.6	1.09	2.6	4.9	0.029
Max	24	1.11	28	57	0.51
Mean	6.6	1.05	2.2	4.1	−0.10
Std dev	2.1	0.06	1.7	3.4	0.19
Skewness	1.6	−1.62	4.4	4.8	−0.19
Excess kurtosis	6.0	7.68	42	51	−0.066
First value	8.4	0.93	3.1	7.2	−0.070
LADCP	5.1	0.90	1.9	6.4	−0.23

because it is so strongly correlated with κ_z ($r = 0.98$) that it does not provide additional information.

Here, κ_z has a mean of 4.1×10^{-4} m^2 s^{-1}, median of 3.3×10^{-4} m^2 s^{-1}, and covers a range from 0.5×10^{-4} to 57×10^{-4} m^2 s^{-1}. At the depths ensonified by the moored ADCP, the spatial section (Fig. 2) has κ_z varying from 0.3×10^{-4} to 20×10^{-4} m^2 s^{-1} with a mean of 3.1×10^{-4} m^2 s^{-1}. The range in the spatial section across Shag Rocks Passage is consistent with the range of the time series, especially given the inherent uncertainty in the method [reported by Polzin et al. (2002) to be around a factor of 3–4].

None of the time series (Fig. 6) display annual or semiannual signals, such as those seen by Large and Van Loon (1989) in Southern Ocean winds. There is no significant correlation between the local wind speed and any of the mooring records (Fig. 6) or the velocity and temperature of the other moorings in Shag Rocks Passage (Table 1 and Fig. 1). The possible influence of the winds or atmospheric pressure (direct or indirect) was further investigated by searching for correlations between κ_z and the wind speed and atmospheric pressure at sea level, bandpass filtered to near-inertial periods, using the ERA-Interim dataset (ECMWF 2009) in the entire region south of 30°S. Lags of up to 80 days were considered. No significant correlations were found.

Table 2 lists statistics of the time series of integrated shear variance, buoyancy frequency, dissipation rate, rotary coefficient, and diffusivity. The agreement is good between the first values of the time series and the LADCP values taken from the nearest station of the deployment cruise and averaged over the same depths observed by the moored ADCP. This station was occupied approximately 7 h before the start of the mooring record. All (except the rotary coefficient) have rather nonnormal distributions, as indicated by their large skewness and excess kurtosis, although the integrated shear variance and buoyancy frequency are much less extreme than ϵ and κ_z. Higher kurtosis indicates that more of the variance is the result of infrequent extreme deviations, as opposed to frequent modestly sized deviations. Averaging over periods of 5 days or more gives a significantly more stable mean. The distribution of κ_z is shown in Fig. 7 and is lognormal, consistent with microstructure turbulence observations (e.g., Gregg et al. 1993).

The time-varying temperature gradient used to calculate the buoyancy frequency affects the calculated κ_z. If we had, instead, used a constant temperature gradient of that measured at the nearest station of the deployment cruise (averaged over the appropriate depths), the range of κ_z would be 0.3×10^{-4} to 62×10^{-4} m^2 s^{-1} with a median of 3.2×10^{-4} m^2 s^{-1}. Using the fit described above to extrapolate temperature but replacing the fit for salinity with the average CTD salinity profile (i.e., not varying salinity with time), the range of κ_z would be 0.5×10^{-4}–54×10^{-4} m^2 s^{-1} with a median of 3.2×10^{-4} m^2 s^{-1}. The time series of κ_z calculated using a constant salinity profile is virtually indistinguishable from that calculated using the fitted salinities.

The distribution of the rotary coefficient (Fig. 8) is approximately normal, as indicated by the low skewness and excess kurtosis, and the mean value of −0.11 indicates weak upward energy propagation at these depths (1800–2400 m). The LADCP-derived rotary coefficient is only just within one standard deviation of the time-series mean but still lies well within the range of the time

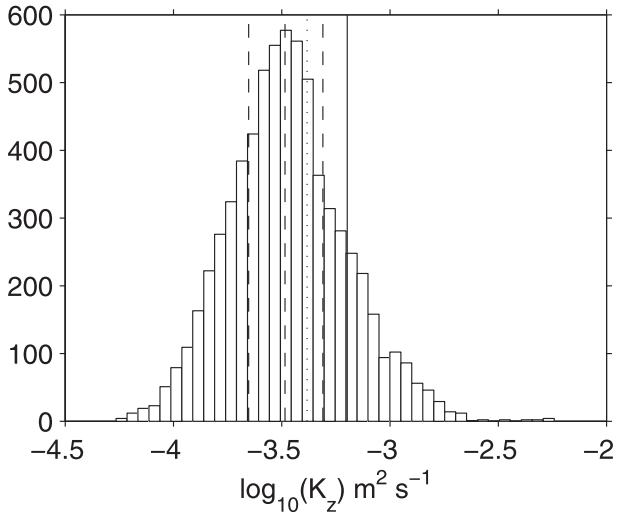

FIG. 7. Distribution of time-series diffusivity. The dashed lines are the 25th, 50th (median), and 75th percentiles; the dotted line is the mean; and the solid line is the diffusivity found by the LADCP, averaged over the water depth observed by the moored ADCP.

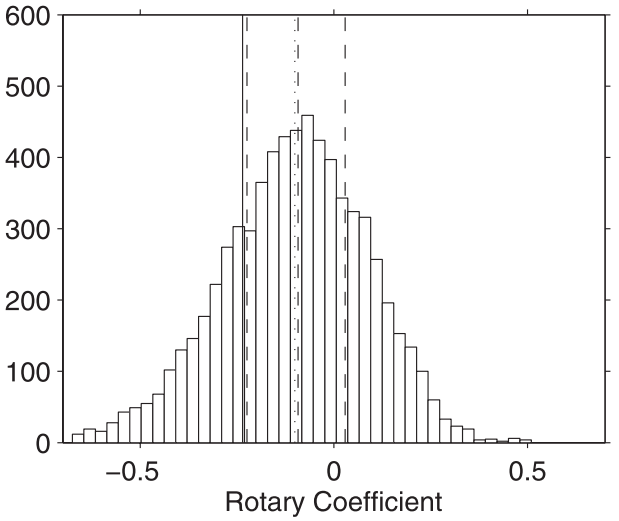

FIG. 8. Distribution of time-series rotary coefficient (RC): the dashed lines are the 25th, 50th (median), and 75th percentiles; the dotted line is the mean; and the solid line is the RC found by the LADCP, averaged over the water depth observed by the moored ADCP.

series. The rotary coefficient is relatively low at the start of the time series (Fig. 6), that is, when the LADCP-derived value was obtained.

Comparison of these time series shows the separate effects of shear and buoyancy frequency in the derivation of κ_z: peaks in integrated shear variance appear as peaks in κ_z (with a particularly strong peak in October 2004), whereas peaks in buoyancy frequency appear as troughs in κ_z. Correlations between the time series (Table 3) show that integrated shear variance and κ_z are strongly correlated, with $r = 0.89$, whereas buoyancy frequency and κ_z are much more weakly anticorrelated ($r = -0.31$), indicating that variations in κ_z are dominated by variations in shear.

The moderately strong correlation between temperature and buoyancy frequency ($r = 0.47$) is apparent in Fig. 6, although, owing to the nature of the fit used (Fig. 4), strong peaks in temperature appear as troughs in buoyancy frequency rather than peaks. The mooring lies very close to the Polar Front (Fig. 2), so we hypothesize that the front may have moved over the mooring, possibly multiple times during the 18-month deployment. The CTD stations confirm that the front moved over the mooring at least once: the deployment cruise CTD closest to mooring Shag2b is the coldest of the profiles (Fig. 4a) and lies to the south of the Polar Front, whereas the recovery cruise CTD, taken at the same location, is within the warmer group to the north of the Polar Front. Smith et al. (2010) observed that the front moved ~1° (65 km) to the west in 11 days during the deployment cruise. The temperature time series is not correlated with the velocity or shear, and the stratification of the CTD stations north and south of the front is similar (the range in buoyancy frequency is small), so the possible movement of the front during the mooring deployment does not have a strong influence on κ_z.

The weak anticorrelation between κ_z and rotary coefficient ($r = -0.40$) suggests that when the rotary coefficient is low, indicating more upward-propagating energy (probably from internal waves generated at the topography), κ_z is high, presumably from more internal wave breaking. Figure 6 reveals coincident troughs in rotary coefficient and peaks in κ_z.

The effects of mooring knockdown and tilt have been considered. From the ADCP pressure record the maximum knockdown of 180 m occurred during a 2-week period of particularly strong currents in May 2003 but, during the rest of the record, the knockdown rarely exceeded 20 m. Similarly the pitch and roll reach maxima of 3° and 5°, respectively, during the same period, but otherwise rarely exceed 1°. These are not thought to have a significant effect on the shear or buoyancy frequency, and thus on κ_z, for two reasons. First, the depth, pitch, and roll are not correlated with shear, buoyancy frequency, or κ_z. Second, we considered what size of knockdown or tilt would be necessary to produce the observed ranges of shear and buoyancy frequency in the absence of varying currents and temperatures. The required knockdowns of nearly 700 m to produce the observed range in shear and over 1500 m to produce the observed range in buoyancy frequency are both greater than the total height of the mooring and far exceed the

TABLE 3. Correlations between the time series of temperature T at 600 mab, integrated shear variance (ISV), buoyancy frequency $\overline{N}$, dissipation rate ϵ, rotary coefficient (RC), and diffusivity κ_z, all after applying the running 24-h mean. Values in bold are significant at the 95% confidence level.

	T	ISV	$\overline{N}$	ϵ	RC	κ_z
T	1	−0.19	**0.47**	−0.23	0.27	−0.26
ISV		1	−0.04	**0.94**	**−0.38**	**0.89**
$\overline{N}$			1	−0.15	0.15	**−0.31**
ϵ				1	**−0.39**	**0.98**
RC					1	**−0.40**
κ_z						1

observed knockdown. Buoyancy frequency will not be affected by the tilt since it is extrapolated from temperature readings at the depth of the ADCP only. The tilt required to produce the observed range in shear is nearly 65°, far greater than the observed range in pitch or roll. We therefore conclude that the variations seen in κ_z are caused by changes in the ocean's turbulent flow and not artifacts of the mooring motion.

4. Spectral analysis

Using the multitaper method (Thomson 1982; Percival and Walden 1993), we performed spectral analysis to search for significant periodicities that could be linked to a particular source of variability. Spectra are shown in Fig. 9 for the northward and eastward depth-mean velocities, temperature at 2400 m, ECMWF reanalysis wind speed at the nearest grid point to mooring Shag2b, integrated shear variance [both with and without the smoothing described in section 3a(4)], buoyancy frequency, and κ_z with the smoothing described in section 3a(4). We include the smoothed integrated shear variance for ease of comparison with the smoothed κ_z. Each plot also shows the theoretical red noise spectrum calculated from the lag-1 autocorrelation coefficient for that variable, except for Fig. 9e, the unsmoothed integrated shear variance. Since many oceanographic quantities are approximately red, this was used as a null hypothesis: peaks in the spectra are considered significantly different from a red noise background if they lie above the 95% confidence limit of the red noise spectrum.

The main diurnal (O_1 and K_1) and semidiurnal (M_2 and S_2) tidal frequencies are visible in the velocities (Figs. 9a,b), particularly in the northward velocity. Very small peaks at the local inertial frequency (0.067 cpd, period 15.0 h) are also present. The spectrum of the integrated shear variance calculated without the smoothing described in section 3a(4) (Fig. 9e) shows that the integrated shear variance is very energetic at high frequencies. This demonstrates the validity of the assumption stated in section 2 that subinertial shear is small compared with that in the internal wave field. Both the unsmoothed integrated shear variance and unsmoothed κ_z (not shown) are energetic at high frequencies but do not display a particularly noticeable increase in activity at inertial, diurnal, or semidiurnal frequencies. Although this might suggest that the inertial and diurnal/semidiurnal tidal components of the velocities are barotropic rather than baroclinic, Sherman and Pinkel (1991) point out that small-scale internal waves (which contribute the most shear) are vertically heaved by other internal waves. This Doppler shifts the encounter frequency as measured by a fixed mooring across frequency space so that the intrinsic frequency of the waves cannot be identified.

The northward (along-stream) velocity shows high spectral energy in a broad band from 10 to 60 days, with a noticeable peak around 14 days, the period of the spring–neap tidal cycle, whereas the eastward (cross-stream) velocity is most energetic in the band from 2 to 5 days, with a particularly large peak at a period of approximately 4 days. Although the wind speed shows variability at periods between 6 h and ~6 days, it is not correlated or coherent with the current velocity, so it is not a direct driver of that variability. Comparison with other Antarctic Circumpolar Current (ACC) current meter velocities suggests that the topographic constriction in the east–west direction is responsible for the difference, in the energetic frequencies, exhibited by the northward and eastward velocities. Bryden and Heath (1985) examined moored current meter data southeast of New Zealand and in central Drake Passage. Phillips and Rintoul (2000) examined moored current meter data in the ACC south of Australia. Both studies suggest that, in areas with topographic constrictions, the cross-stream velocity tends to exhibit variability at shorter periods than the along-stream velocity. The spectrum of the temperature time series shows rather different behavior to the velocities, with low variability at high frequencies but a significant peak at periods of ~50–100 days. This is comparable to the temperature spectra found by Bryden and Heath (1985) and Phillips and Rintoul (2000).

The variability at periods of 10–20 days in the spectra of integrated shear variance and buoyancy frequency, and thus κ_z and rotary coefficient (spectrum not shown but broadly similar to the spectra of κ_z and integrated shear variance), is most likely due to the spring–neap tidal cycle combined with eddy activity: several authors have reported eddy activity as being important at these periods (Bryden 1979; Sciremammano 1980; Bryden and Heath 1985).

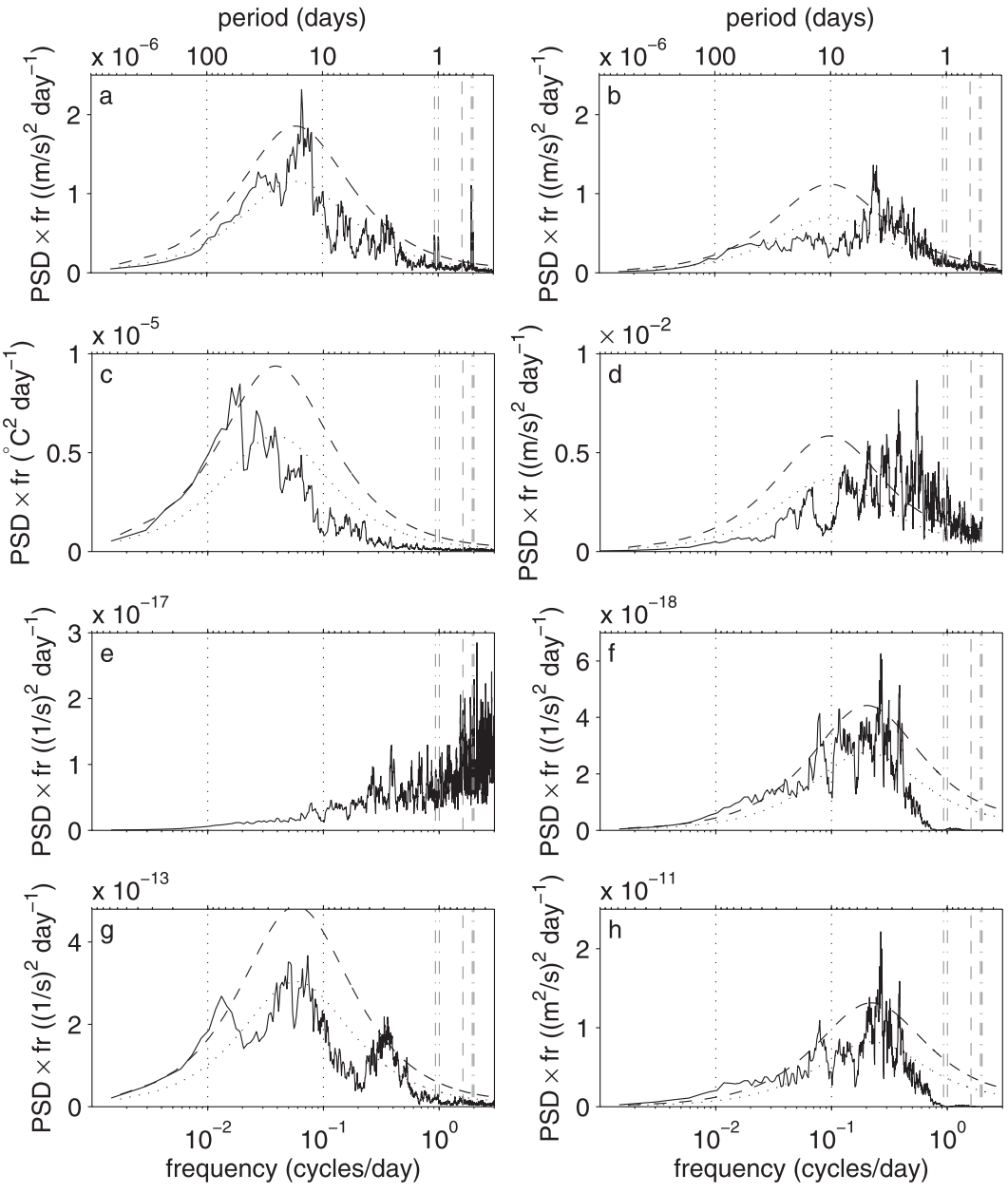

FIG. 9. Variance preserving spectra: in each plot the vertical axis is the power spectral density (PSD) × frequency (fr). The dotted curve is the theoretical red noise spectrum based on the lag-1 autocorrelation coefficient, and the dashed curve is the 95% confidence limit. The vertical dashed line is the inertial frequency, and the vertical dotted–dashed lines are the main diurnal and semidiurnal tidal frequencies (O_1, K_1, M_2, and S_2 from left to right, although M_2 and S_2 are very close together and so may appear as one thick dotted–dash line). Spectra are (a) northward and (b) eastward depth-mean velocity (these are largely representative of the spectra for individual levels as the currents in this area are quite barotropic); (c) temperature from the instrument located 600 mab; (d) six-hourly ECMWF reanalysis wind speed at the nearest grid point to mooring Shag2b; integrated shear variance (ISV) (e) without the smoothing and (f) with the smoothing described in section 3a(4); (g) buoyancy frequency; and (h) κ_z with the smoothing described in section 3a(4).

The large peak at a period of 3.8 days seen in the spectra of eastward velocity, integrated shear variance, and κ_z is particularly unexpected. Bandpass filtering reveals that the signal is very persistent, appearing throughout the κ_z record, with an average amplitude of approximately 1.5×10^{-4} m^2 s^{-1}. It is not an instrumental fault, as the same signal appears in the velocities recorded by the RCMs below the ADCP. It is

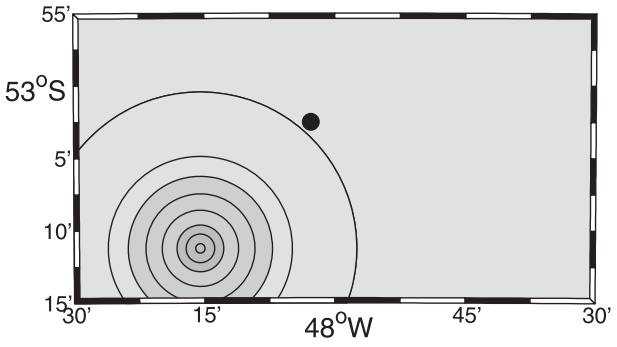

FIG. 10. Idealized axisymmetric seamount used with the Brink model, for comparison with Fig. 1d. Contour intervals are every 200 m with shading every 600 m in the same shading density as in Fig. 1d. The black circle is mooring Shag2b.

not directly wind driven, as the winds are neither correlated nor coherent with κ_z. Moreover, wind driving would be expected to be apparent over a fairly wide area, and the velocities at moorings Shag1 and Shag3 (Fig. 1c and Table 1) do not show a signal at that period. It is not caused by seiching, as the constricted channel is too short in the north–south direction and too wide in the east–west direction to set up such a resonance. In 4 days, water is advected north by an average of 60 km, which is more than the north–south length of the constriction. Bandpass filtering the velocities and plotting a progressive vector diagram (not shown) reveals that this east–west oscillation has an amplitude of approximately 5 km. This is too great to be caused by mooring motion since the ADCP is only 600 m off the seafloor, and spectra of the mooring's depth, pitch, and roll do not reveal a large 3.8-day signal. One remaining possibility is topographically trapped Rossby waves propagating around the local seamount. The mooring is located on the north–east flank of a seamount (Figs. 1c and 2) with a radius of ~15 km at its base and a slope of ~55 m km^{-1}. LeBlond and Mysak (1978) state that wave trapping by a cylindrical seamount (i.e., a seamount with vertical sides) is only possible if the radius of the seamount is greater than the barotropic Rossby radius (1300 km in Shag Rocks Passage, which is much greater than the radius of this seamount). However, subinertial waves can be trapped by a seamount with sloping sides (Rhines 1969; Brink 1989; Sanson 2010) even if the radius of the seamount is less than the barotropic Rossby radius.

Using the model of Brink (1989) with the stratification observed during the deployment cruise and an idealized, axisymmetric seamount (Fig. 10) of similar height, radius, and slope to the one immediately west of the mooring, we find trapped waves with azimuthal wavenumber $n = 1$ and frequency 3.0×10^{-6} s^{-1} (period 3.8 days), consistent with the observed primary peak in the κ_z spectrum of 3.8 days (Model downloaded on 20 Jun 2011 from http://www.whoi.edu/page.do?pid=23361). At $n = 2$ the model finds a trapped wave with a frequency of 4.5×10^{-6} s^{-1} (period 2.6 days), consistent with the second most prominent peak in the spectrum of κ_z. Although the velocities in Figs. 9a,b do not have obvious peaks at a period of 2.6 days, these are the spectra of the depth-mean velocities, that is, the barotropic component. The integrated shear variance (Fig. 9f) has peaks at periods of 3.8 and 2.6 days, indicating that these are baroclinic motions. Such baroclinic motions can increase the internal wave shear variance and thus κ_z.

5. Conclusions

An 18-month time series of internal-wave-driven diapycnal diffusivity from Shag Rocks Passage was inferred from finescale shear using a method modified from that used to calculate κ_z from LADCP shears. The mean κ_z was 4.1×10^{-4} m^2 s^{-1}, consistent with the value obtained from the LADCP data of 6.4×10^{-4} m^2 s^{-1} at the depths ensonified by the moored ADCP. The value of κ_z varies by a factor of just over 100, much greater than the factor of 3–4 uncertainty inherent in the method (Polzin et al. 2002), from 0.5×10^{-4} to 57×10^{-4} m^2 s^{-1}. This range is slightly greater than the spatial variability seen in Shag Rocks Passage at the same depths as ensonified by the moored ADCP. The record shows no obvious annual or semiannual cycle, despite being at a high latitude where seasonality is often quite marked. The record displays variability over time scales from 10 to 20 days, thought to be driven by eddy activity and the spring–neap tidal cycle, and variability at periods of 3.8 and 2.6 days most likely due to topographically trapped waves propagating around the local seamount. The quantity κ_z is anticorrelated with the rotary coefficient (indicating that stronger mixing occurs during times of upward energy propagation), which suggests that mixing occurs due to the breaking of internal waves generated at topography. We have demonstrated that time series can, to an extent, shed light on the mechanisms causing mixing.

The results presented here are from a single moored ADCP in a rather atypical location where a strong flow is extremely constrained by the topography. The moorings used were not designed to measure κ_z, but we have demonstrated that the method used to calculate κ_z from CTD/LADCP profiles can be adapted for use with moored instruments. If measuring κ_z were the aim, then in regions with a less stable temperature–salinity relationship, or where a linear temperature gradient is not an appropriate assumption, the moorings would need to

include temperature and salinity sensors spanning the depth range ensonified by the moored ADCP. It is also necessary to program the ADCP to provide both sufficient vertical resolution and enough depth bins to perform a Fourier transform in the vertical. The vertical sampling frequency must be at least twice the largest wavenumber included in the integration; that is, the length of the depth bins must be, at most, half the smallest wavelength included. Moreover, finescale parameterizations have not been assessed for depth bins greater than 20 m. We would therefore recommend using depth bins of no more than 20–40 m. The decision on what constitutes ''enough'' depth bins is rather heuristic, but we would recommend a minimum of 15–20 bins of good data (i.e., after the data quality control cuts, such as that based on the percentage of good beam solutions, have been made).

Time series at other locations will be important in assessing whether diapycnal mixing commonly varies over a similar range or whether this is simply a feature of this particular location. In the Scotia Sea region, there is considerable atmospheric variability such as storms and seasonal cycles, and, in the ocean, variability includes extensive eddy activity, strong currents, and movement of fronts. Shag Rocks Passage has complex topography with which varying water motions can interact. We postulate that other regions with less atmospheric and oceanic variability and less complex topography may experience less temporal variability in κ_z at the depths observed here. We are therefore cautiously optimistic about the validity of ''snapshots'' of κ_z, though we would prefer to see further studies of temporal variability over at least a year at a range of locations, especially since local topography (e.g., small seamounts) can provide variability on time scales unrelated to large-scale atmospheric forcing.

Acknowledgments. The CTD, LADCP, and mooring data were acquired as part of the North Scotia Ridge Overflow project, funded by the Natural Environment Research Council Grant NER/G/S/2001/00006 through the Antarctic Funding Initiative. A Natural Environment Research Council Ph.D. studentship at UEA supported G.M.D. during the analysis and writing of this report. We thank Gareth Janacek and Adrian Matthews for useful discussions on spectral analysis and our anonymous reviewers for their insightful comments. The ERA-Interim data were obtained from ECMWF (at http://www.ecmwf.int/research/era/do/get/index). The Brink model is made available online (at http://www.whoi.edu/page.do?pid=23361). Alex Tate kindly provided multibeam bathymetry from the British Antarctic Survey Marine Geophysical Database.

REFERENCES

Alford, M. H., 2001: Internal swell generation: The spatial distribution of energy flux from the wind to mixed layer near-inertial motions. *J. Phys. Oceanogr.,* **31,** 2359–2368.

——, 2003a: Improved global maps and 54-year history of wind-work on ocean inertial motions. *Geophys. Res. Lett.,* **30,** 1424, doi:10.1029/2002GL016614.

——, 2003b: Redistribution of energy available for ocean mixing by long-range propagation of internal waves. *Nature,* **423,** 159–162.

Arhan, M., A. C. Naveira Garabato, K. J. Heywood, and D. P. Stevens, 2002: The Antarctic Circumpolar Current between the Falkland Islands and South Georgia. *J. Phys. Oceanogr.,* **32,** 1914–1931.

Baines, P. G., 1973: Generation of internal tides by flat-bump topography. *Deep-Sea Res.,* **20,** 179–205.

——, 1982: On internal tide generation models. *Deep-Sea Res.,* **29,** 307–338.

Bell, T. H., 1975: Topographically generated internal waves in open ocean. *J. Geophys. Res.,* **80,** 320–327.

Brink, K. H., 1989: The effect of stratification on seamount-trapped waves. *Deep-Sea Res.,* **36,** 825–844.

Bryden, H. L., 1979: Poleward heat-flux and conversion of available potential-energy in Drake Passage. *J. Mar. Res.,* **37**, 1–22.

——, and R. A. Heath, 1985: Energetic eddies at the northern edge of the Antarctic Circumpolar Current in the southwest Pacific. *Prog. Oceanogr.,* **14** (1–4), 65–87.

D'Asaro, E. A., 1984: Wind forced internal waves in the North Pacific and Sargasso Sea. *J. Phys. Oceanogr.,* **14,** 781–794.

ECMWF, cited 2009: ECMWF ERA-Interim re-analysis data. European Centre for Medium-Range Weather Forecasts British Atmospheric Data Centre. [Available online at http://badc.nerc.ac.uk/data/ecmwf-era-interim/.]

Garrett, C., and W. Munk, 1975: Space–time scales of internal waves: A progress report. *J. Geophys. Res.,* **80,** 291–297.

——, and L. St. Laurent, 2002: Aspects of deep ocean mixing. *J. Oceanogr.,* **58,** 11–24.

——, and E. Kunze, 2007: Internal tide generation in the deep ocean. *Annu. Rev. Fluid Mech.,* **39,** 57–87.

Gonella, J., 1972: Rotary-component method for analyzing meteorological and oceanographic vector time series. *Deep-Sea Res.,* **19,** 833–846.

Gregg, M. C., and E. Kunze, 1991: Shear and strain in Santa-Monica Basin. *J. Geophys. Res.,* **96** (C9), 16 709–16 719.

——, H. E. Seim, and D. B. Percival, 1993: Statistics of shear and turbulent dissipation profiles in random internal wave fields. *J. Phys. Oceanogr.,* **23,** 1777–1799.

——, T. B. Sanford, and D. P. Winkel, 2003: Reduced mixing from the breaking of internal waves in equatorial waters. *Nature,* **422,** 513–515.

Henyey, F. S., J. Wright, and S. M. Flatte, 1986: Energy and action flow through the internal wave field: An eikonal approach. *J. Geophys. Res.,* **91** (C7), 8487–8495.

Heywood, K. J., A. C. Naveira Garabato, and D. P. Stevens, 2002: High mixing rates in the abyssal Southern Ocean. *Nature,* **415,** 1011–1014.

——, J. L. Collins, C. W. Hughes, and I. Vassie, 2007: On the detectability of internal tides in Drake Passage. *Deep-Sea Res.,* **54,** 1972–1984.

Inall, M. E., T. P. Rippeth, and T. J. Sherwin, 2000: Impact of nonlinear waves on the dissipation of internal tidal energy at a shelf break. *J. Geophys. Res.,* **105** (C4), 8687–8705.

Jackett, D. R., and T. J. McDougall, 1997: A neutral density variable for the world's oceans. *J. Phys. Oceanogr.,* **27,** 237–263.

Kunze, E., 1985: Near-inertial wave propagation in geostrophic shear. *J. Phys. Oceanogr.,* **15,** 544–565.

——, and T. B. Sanford, 1984: Observations of near-inertial waves in a front. *J. Phys. Oceanogr.,* **14,** 566–581.

——, A. J. Williams, and M. G. Briscoe, 1990: Observations of shear and vertical stability from a neutrally buoyant float. *J. Geophys. Res.,* **95** (C10), 18 127–18 142.

——, E. Firing, J. M. Hummon, T. K. Chereskin, and A. M. Thurnherr, 2006: Global abyssal mixing inferred from lowered ADCP shear and CTD strain profiles. *J. Phys. Oceanogr.,* **36,** 1553–1576.

Large, W. G., and H. Van Loon, 1989: Large-scale, low-frequency variability of the 1979 FGGE surface buoy drifts and winds over the Southern Hemisphere. *J. Phys. Oceanogr.,* **19,** 216–232.

LeBlond, P., and L. Mysak, 1978: *Waves in the Ocean*. Elsevier, 602 pp.

Ledwell, J. R., A. J. Watson, and C. S. Law, 1998: Mixing of a tracer in the pycnocline. *J. Geophys. Res.,* **103** (C10), 21 499–21 529.

Mauritzen, C., K. L. Polzin, M. S. McCartney, R. C. Millard, and D. E. West-Mack, 2002: Evidence in hydrography and density fine structure for enhanced vertical mixing over the Mid-Atlantic Ridge in the western Atlantic. *J. Geophys. Res.,* **107,** C103147, doi:10.1029/2001JC001114.

McComas, C. H., and P. Muller, 1981: The dynamic balance of internal waves. *J. Phys. Oceanogr.,* **11,** 970–986.

Moore, J. K., M. R. Abbott, and J. G. Richman, 1997: Variability in the location of the Antarctic Polar Front (90°–20°W) from satellite sea surface temperature data. *J. Geophys. Res.,* **102** (C13), 27 825–27 833.

Moum, J. N., and J. D. Nash, 2009: Mixing measurements on an equatorial ocean mooring. *J. Atmos. Oceanic Technol.,* **26,** 317–336.

Munk, W., and C. Wunsch, 1998: Abyssal recipes II: Energetics of tidal and wind mixing. *Deep-Sea Res.,* **45,** 1977–2010.

Naveira Garabato, A. C., E. L. McDonagh, D. P. Stevens, K. J. Heywood, and R. J. Sanders, 2002: On the export of Antarctic Bottom Water from the Weddell Sea. *Deep-Sea Res.,* **49,** 4715–4742.

——, D. P. Stevens, and K. J. Heywood, 2003: Water mass conversion, fluxes, and mixing in the Scotia Sea diagnosed by an inverse model. *J. Phys. Oceanogr.,* **33,** 2565–2587.

——, K. L. Polzin, B. A. King, K. J. Heywood, and M. Visbeck, 2004: Widespread intense turbulent mixing in the Southern Ocean. *Science,* **303,** 210–213.

Nikurashin, M., and R. Ferrari, 2010a: Radiation and dissipation of internal waves generated by geostrophic motions impinging on small-scale topography: Application to the Southern Ocean. *J. Phys. Oceanogr.,* **40,** 2025–2042.

——, and ——, 2010b: Radiation and dissipation of internal waves generated by geostrophic motions impinging on small-scale topography: Theory. *J. Phys. Oceanogr.,* **40,** 1055–1074.

Olbers, D., 1998: Comments on ''On the obscurantist physics of 'form drag' in theorizing about the Circumpolar Current.'' *J. Phys. Oceanogr.,* **28,** 1647–1654.

Orsi, A. H., T. Whitworth, and W. D. Nowlin, 1995: On the meridional extent and fronts of the Antarctic Circumpolar Current. *Deep-Sea Res.,* **42,** 641–673.

Osborn, T. R., 1980: Estimates of the local-rate of vertical diffusion from dissipation measurements. *J. Phys. Oceanogr.,* **10,** 83–89.

Palmer, M. R., T. P. Rippeth, and J. H. Simpson, 2008: An investigation of internal mixing in a seasonally stratified shelf sea. *J. Geophys. Res.,* **113,** C12005, doi:10.1029/2007JC004531.

Percival, D., and A. Walden, 1993: *Spectral Analysis for Physical Applications: Multitaper and Conventional Univariate Techniques*. Cambridge University Press, 583 pp.

Phillips, H. E., and S. R. Rintoul, 2000: Eddy variability and energetics from direct current measurements in the Antarctic Circumpolar Current south of Australia. *J. Phys. Oceanogr.,* **30,** 3050–3076.

Pollard, R. T., 1970: On generation by winds of inertial waves in ocean. *Deep-Sea Res.,* **17,** 795–812.

——, and R. C. Millard, 1970: Comparison between observed and simulated wind-generated inertial oscillations. *Deep-Sea Res.,* **17,** 813–821.

Polzin, K. L., and Y. V. Lvov, 2011: Towards regional characterizations of the oceanic internal wavefield. *Rev. Geophys.,* **49,** RG4003, doi:10.1029/2010RG000329.

——, J. M. Toole, and R. W. Schmitt, 1995: Finescale parameterizations of turbulent dissipation. *J. Phys. Oceanogr.,* **25,** 306–328.

——, ——, J. R. Ledwell, and R. W. Schmitt, 1997: Spatial variability of turbulent mixing in the abyssal ocean. *Science,* **276,** 93–96.

——, E. Kunze, J. Hummon, and E. Firing, 2002: The finescale response of lowered ADCP velocity profiles. *J. Atmos. Oceanic Technol.,* **19,** 205–224.

Rhines, P. B., 1969: Slow oscillations in an ocean of varying depth. Part 2. Islands and seamounts. *J. Fluid Mech.,* **37,** 191–205.

Rippeth, T. P., E. Williams, and J. H. Simpson, 2002: Reynolds stress and turbulent energy production in a tidal channel. *J. Phys. Oceanogr.,* **32,** 1242–1251.

Sanson, L. Z., 2010: Solutions of barotropic trapped waves around seamounts. *J. Fluid Mech.,* **661,** 32–44.

Sciremammano, F., 1980: The nature of the poleward heat-flux due to low-frequency current fluctuations in Drake Passage. *J. Phys. Oceanogr.,* **10,** 843–852.

Sherman, J. T., and R. Pinkel, 1991: Estimates of the vertical wavenumber–frequency spectra of vertical shear and strain. *J. Phys. Oceanogr.,* **21,** 292–303.

Shroyer, E. L., J. N. Moum, and J. D. Nash, 2010: Vertical heat flux and lateral mass transport in nonlinear internal waves. *Geophys. Res. Lett.,* **37,** L08601, doi:10.1029/2010GL042715.

Sloyan, B. M., 2005: Spatial variability of mixing in the Southern Ocean. *Geophys. Res. Lett.,* **32,** L18603, doi:10.1029/2005GL023568.

Smith, I. J., D. P. Stevens, K. J. Heywood, and M. P. Meredith, 2010: The flow of the Antarctic Circumpolar Current over the North Scotia Ridge. *Deep-Sea Res.,* **57,** 14–28.

Smith, W. H. F., and D. T. Sandwell, 1997: Global sea floor topography from satellite altimetry and ship depth soundings. *Science,* **277,** 1956–1962.

St. Laurent, L., and C. Garrett, 2002: The role of internal tides in mixing the deep ocean. *J. Phys. Oceanogr.,* **32,** 2882–2899.

Thomson, D. J., 1982: Spectrum estimation and harmonic-analysis. *J. Proc. IEEE,* **70,** 1055–1096.

Thorpe, S. A., 1992: The generation of internal waves by flow over the rough topography of a continental slope. *Proc. Roy. Soc. London,* **439,** 115–130.

——, 2005: *The Turbulent Ocean*. Cambridge University Press, 439 pp.

Toole, J. M., K. L. Polzin, and R. W. Schmitt, 1994: Estimates of diapycnal mixing in the abyssal ocean. *Science,* **264,** 1120–1123.

Walkden, G. J., K. J. Heywood, and D. P. Stevens, 2008: Eddy heat fluxes from direct current measurements of the Antarctic Polar Front in Shag Rocks Passage. *Geophys. Res. Lett.,* **35,** L06602, doi:10.1029/2007GL032767.

Wunsch, C., and R. Ferrari, 2004: Vertical mixing, energy and the general circulation of the oceans. *Annu. Rev. Fluid Mech.,* **36,** 281–314.